electronics

MDPI

Article

Research on FOPID Controller and CMOPSO Optimization for Prevention and Control of Oscillatory Instability at the PCC in a Hydro–Wind–Photovoltaic Grid-Connected System

Bojin Tang [1,2], Weiwei Yao [1,2], Teng Yi [1,3], Rui Lv [1,3], Zhi Wang [4] and Chaoshun Li [4,*]

[1] Laboratory of Hydro-Wind-Solar Multi-Energy Control Coordination, Wuhan 430014, China
[2] Institute of Science and Technology, China Three Gorges Corporation, Beijing 101100, China
[3] China Yangtze Power Co., Ltd., Wuhan 430014, China
[4] Institute of Water Resources and Hydropower Research, Huazhong University of Science and Technology, Wuhan 430074, China
* Correspondence: csli@hust.edu.cn

Abstract

To address the key problems of low-frequency oscillation and insufficient regulation accuracy at the Point of Common Coupling (PCC) in hydro–wind–photovoltaic hybrid systems, which are caused by the randomness of wind and photovoltaic output, the water-hammer effect of hydropower units, and multi-source power coupling, a joint control strategy based on Fractional-Order Proportional Integral Derivative (FOPID) and Co-evolutionary Multi-objective Particle Swarm Optimization (CMOPSO) is proposed. First, a small-signal transfer function model of the system covering photovoltaic inverters, doubly fed induction generators (DFIGs), hydropower units and voltage-source converter-based high-voltage direct current (VSC-HVDC) converter stations is established to accurately characterize the water-hammer effect and multi-source dynamic coupling characteristics. Second, a Caputo-type FOPID controller is designed. Compared with traditional integer-order controllers with limited tuning flexibility, the FOPID controller utilizes its five degrees of freedom to address specific multi-source coupling challenges. This precisely compensates for the non-minimum phase lag caused by the water-hammer effect in hydropower units via the fractional derivative link, and effectively smooths the impact of stochastic wind–solar fluctuations on PCC voltage through the memory characteristics of the fractional integral link. This multi-parameter regulation mechanism prevents a trade-off between response speed and overshoot suppression, achieving effective decoupling of complex multi-source dynamic interactions. Third, a dual-objective optimization framework with the Integral of Time-weighted Absolute Error (ITAE) and Oscillatory Disturbance Risk Index (ODRI) as the objectives is constructed. The multi-population co-evolution mechanism of the CMOPSO algorithm is adopted to solve the Pareto-optimal solution set, realizing the coordinated optimization of dynamic response accuracy and oscillation instability risk. Finally, comparative simulations are carried out on the Simulink platform with traditional PI/FOPI controllers and optimization algorithms such as Multi-objective Particle Swarm Optimization based on the Decomposition/Simple Indicator-Based Evolutionary Algorithm (MPSOD/SIBEA). The results show that the proposed strategy can effectively suppress low-frequency oscillations in the range of 0~30 Hz. Compared with the traditional PI controller, the PCC voltage overshoot is reduced by more than 40%, the oscillation decay time is shortened by 33%, the ITAE and ODRI indices are decreased by 12.58% and 2.47%, respectively, and the stability of DC bus voltage is significantly improved. Its robustness and comprehensive control performance are superior to existing methods, providing an efficient and stable control scheme for power electronics-dominated complex new energy grid-connected systems.

Check for updates

Academic Editor: Fabio Corti

Received: 1 April 2026
Revised: 3 May 2026
Accepted: 11 May 2026
Published: 14 May 2026

Copyright: © 2026 by the authors. Licensee MDPI, Basel, Switzerland. This article is an open access article distributed under the terms and conditions of the Creative Commons Attribution (CC BY) license.

Keywords: hydro–wind–photovoltaic hybrid system; point of common coupling; fractional-order PID controller; oscillatory disturbance risk index

1. Introduction

1.1. Research Background

Driven by global carbon neutrality targets and energy transition strategies, large-scale renewable energy integration has become a dominant trend in modern power systems. Recent reports indicate that renewable energy generation capacity continues to grow rapidly and will dominate newly installed global power capacity in the coming decade [1]. Among renewable resources, hydropower, wind power, and photovoltaic (PV) power generation exhibit strong complementary characteristics in terms of temporal and spatial output profiles [2]. In recent years, hydro–wind–photovoltaic hybrid systems have attracted extensive research attention due to their ability to utilize hydropower's fast regulation capability to mitigate wind and solar intermittency [3]. Several recent studies confirm that coordinated operation of hybrid renewable systems significantly enhances renewable accommodation capability and operational flexibility [4].

The Point of Common Coupling (PCC) serves as the critical interface between hybrid renewable generation systems and the main grid, undertaking power exchange and voltage/frequency regulation functions. With increasing renewables penetration, modern power systems are gradually evolving into low-inertia, converter-dominated systems [5]. Reduced synchronous inertia weakens frequency stability and increases the vulnerability of the system to disturbances [6]. Recent investigations highlight that low-inertia grids exhibit faster frequency dynamics and reduced damping margins compared with conventional power systems [7].

In converter-dominated systems, dynamic interactions between grid-connected inverters and grid impedance introduce new oscillatory modes [8]. Studies conducted in recent years demonstrate that renewable-dominated grids are prone to low-frequency oscillations in the 0–30 Hz range, especially under weak-grid conditions [9]. For wind farms employing DFIG and full-scale converter technologies, small-signal stability analysis reveals complex electromechanical coupling effects that may amplify oscillation risks [10]. Impedance-based stability analysis methods further show that improper converter parameter tuning may trigger resonance and instability phenomena [11].

In hydro–wind–photovoltaic hybrid systems, the nonlinear hydraulic dynamics of hydropower units, including water-hammer effects, further complicate system stability characteristics [12]. Conventional integer-order PI controllers, though widely used in industrial applications, lack sufficient flexibility to cope with strong nonlinear and time-varying disturbances in hybrid renewable systems [13]. To enhance control adaptability, fractional-order control theory has gained renewed attention in recent years. Recent applications demonstrate that fractional-order Proportional Integral/Fractional-Order Proportional Integral Derivative (PI/FOPID) controllers provide superior robustness and enhanced damping capability in renewable-integrated systems [14]. Comparative studies show that fractional-order controllers outperform classical integer-order controllers in handling nonlinear dynamics and improving disturbance rejection performance [15].

Meanwhile, PCC regulation requires simultaneous optimization of multiple conflicting objectives, including voltage tracking accuracy and oscillation damping performance. Multi-objective evolutionary optimization techniques have been widely applied to renewable energy systems in recent years [16]. Advanced Multi-Objective Particle Swarm Optimization (MOPSO) variants have shown strong global search capability and Pareto-

front diversity preservation [17]. Recent developments in co-evolutionary multi-objective algorithms further enhance optimization efficiency and convergence performance [18]. In addition, robust frequency-control strategies under high renewables penetration have become a major research focus [19]. Coordinated optimization frameworks combining advanced controllers and evolutionary algorithms demonstrate improved stability performance compared with traditional tuning methods [20]. Accurate dynamic modeling of converter-interfaced renewable systems is also essential for effective optimization and stability analysis [21].

Despite significant recent progress, an integrated framework that simultaneously considers multi-source coupling dynamics, quantitative oscillation risk assessment, and coordinated fractional-order parameter optimization for PCC in hydro–wind–photovoltaic hybrid systems remains insufficiently investigated.

1.2. Literature Review

Research on the stability control of renewable-integrated power systems has mainly focuses on three aspects: system modeling and dynamic analysis, advanced control strategies, and multi-objective optimization methods.

In terms of system modeling, small-signal modeling and transfer function analysis are widely used to describe the dynamic behavior of renewable energy systems. Existing studies have modeled photovoltaic inverters, DFIG-based wind turbines, and hydropower units individually. However, the coupling effects among multiple energy sources, especially under the influence of hydraulic dynamics such as water hammer, are often neglected, leading to insufficient accuracy in system-level dynamic analysis.

Regarding control strategies, conventional PI controllers remain the dominant choice in industrial applications due to their simplicity and ease of implementation. However, their limited parameter flexibility restricts their performance under nonlinear and time-varying conditions. To address this issue, fractional-order controllers, including Fractional-Order Proportional Integral (FOPI) and FOPID, have been proposed. These controllers introduce additional fractional-order parameters, significantly enhancing the control degrees of freedom and enabling better adaptation to complex system dynamics [22].

From the perspective of optimization methods, multi-objective optimization algorithms have been extensively applied to controller parameter tuning. Classical approaches such as PSO and GA have achieved certain success, but they often suffer from premature convergence and the limited diversity of Pareto solutions. Recently, improved MOPSO algorithms and co-evolutionary strategies have been developed, demonstrating better global search capability and convergence performance. Nevertheless, most existing studies focus on single-objective optimization or lack a unified framework that integrates control design with oscillation risk evaluation.

In addition, although some studies have addressed frequency stability and oscillation suppression in renewable systems, quantitative evaluation metrics for oscillation risk are still insufficient. Most analyses rely on qualitative observations or single performance indices, which cannot comprehensively reflect system stability characteristics.

1.3. Research Gap and Novelty

Although significant progress has been achieved, several critical challenges remain:

(1) Insufficient multi-source coupling modeling. Existing models often simplify or neglect the dynamic coupling among hydropower, wind, and photovoltaic subsystems, particularly ignoring nonlinear hydraulic effects such as water hammer. This limits the accuracy of system stability analysis at the PCC.

(2) Limited adaptability of conventional controllers. Traditional integer-order PI controllers lack sufficient flexibility to cope with strong nonlinearities and time-varying disturbances in hybrid renewable systems, resulting in inadequate damping performance under complex operating conditions.
(3) Lack of quantitative oscillation risk assessment frameworks. Most studies focus on voltage or frequency deviations without explicitly quantifying oscillation instability risks, making it difficult to perform systematic stability evaluation and optimization.
(4) Inadequate integration of control and optimization strategies. Existing approaches often treat controller design and parameter optimization separately, lacking a unified framework that simultaneously considers multi-objective performance and system dynamics.

To address these challenges, this paper proposes a FOPID–CMOPSO coordinated optimization framework with the following main contributions:

(1) Multi-source coupled dynamic modeling. A comprehensive small-signal transfer function model is established for hydro–wind–photovoltaic hybrid systems, incorporating photovoltaic inverters, DFIG units, hydropower units, and VSC-HVDC systems, while explicitly considering water-hammer effects and multi-source coupling dynamics.
(2) Fractional-order controller design. Caputo-type FOPI and FOPID controllers are designed to enhance control flexibility and improve system adaptability to nonlinear and time-varying disturbances.
(3) Dual-objective optimization framework. A multi-objective optimization model is constructed using Integral of Time-weighted Absolute Error (ITAE) and Oscillatory Disturbance Risk Index (ODRI), enabling quantitative evaluation of both dynamic performance and stability.
(4) CMOPSO-based parameter optimization. A Co-evolutionary Multi-Objective Particle Swarm Optimization (CMOPSO) algorithm is employed to obtain a well-distributed Pareto-optimal solution set with improved convergence and diversity.
(5) Comprehensive validation. The effectiveness and superiority of the proposed method are verified through Simulink simulations, with comparisons against conventional PI controllers and other optimization algorithms such as Multi-objective Particle Swarm Optimization based on Decomposition (MPSOD) and the Simple Indicator-Based Evolutionary Algorithm (SIBEA).

2. System Modeling of Hydro–Wind–Solar Grid-Connected System

2.1. Overall System Topology

The topology of the hydro–wind–photovoltaic hybrid system with VSC-HVDC transmission studied in this paper is illustrated in Figure 1. The system is mainly composed of a hydropower station cluster in a certain river basin, a photovoltaic power plant and a wind farm. Each subsystem is connected to the 500 kV AC bus through power electronic converters and integrated at the PCC [23]. The collected electric energy is transmitted to the receiving-end power grid via the Line-Commutated Converter-based High-Voltage Direct Current (LCC-HVDC) system, while local load consumption is also ensured. This architecture leverages the active power regulation capability of hydropower units to mitigate fluctuations in wind and photovoltaic output, thus maintaining the voltage and frequency stability of the PCC.

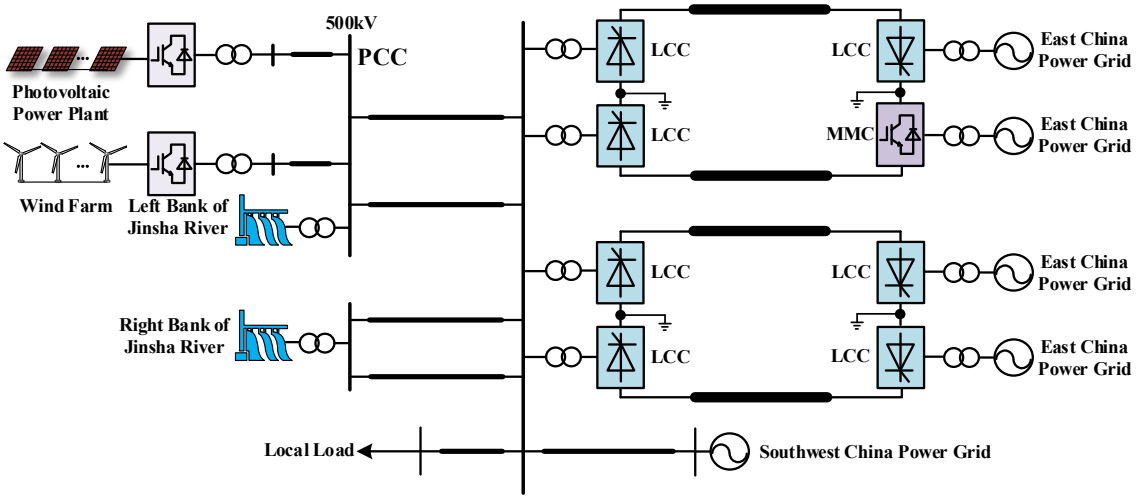


Figure 1. Model topology diagram.

2.2. Transfer-Function Modeling of Subsystems

2.2.1. Transfer-Function Model of Photovoltaic Inverter

The photovoltaic system adopts a grid-connected control strategy of a Maximum Power Point Tracking (MPPT) outer loop plus current inner loop, and its transfer function model under small-signal conditions is given as follows [24]:

MPPT loop: The dynamic characteristics of the perturb-and-observe method are approximated as a first-order inertial link:

$$G_{\mathrm{MPPT}}(s) = \frac{1}{1 + T_{\mathrm{MPPT}} s} \tag{1}$$

where T_{MPPT} is the MPPT dynamic time constant (set to 0.1 s). The value of 0.1 s is selected based on common engineering practice to ensure the MPPT response is sufficiently fast relative to the 0.5–2 Hz oscillation frequency, while maintaining numerical stability in the small-signal model.

Current inner loop: A PI controller is adopted, combined with the AC-side Inductance–Capacitance (LC) filter (inductance Lf, capacitance Cf). The transfer function of current control is expressed as [8]

$$G_{\mathrm{PI}\text{-}i}(s) = K_{\mathrm{p}\text{-}i} + \frac{K_{\mathrm{i}\text{-}i}}{s} \tag{2}$$

$$G_{\mathrm{LC}}(s) = \frac{1}{L_f C_f s^2 + 1} \tag{3}$$

The transfer function of the current injected into the PCC by the photovoltaic system is the series connection of each link:

$$G_{\mathrm{PV}}(s) = G_{\mathrm{MPPT}}(s) \cdot G_{\mathrm{PI}\text{-}i}(s) \cdot G_{\mathrm{LC}}(s) \tag{4}$$

2.2.2. Transfer Function Model of DFIG

The DFIG regulates active/reactive power via the rotor-side converter (RSC) and stabilizes the DC bus through the grid-side converter (GSC). This section focuses on the power injection dynamics of the RSC into the PCC: RSC active-power control loop: Current loop PI controller combined with electromagnetic torque dynamics:

$$G_{\mathrm{PI}\text{-}r}(s) = K_{\mathrm{p}\text{-}r} + \frac{K_{\mathrm{i}\text{-}r}}{s} \tag{5}$$

$$G_{\mathrm{Te}}(s) = K_{\mathrm{te}} \tag{6}$$

where K_{te} is the proportional coefficient from rotor current to electromagnetic torque (determined by motor parameters).

Wind turbine aerodynamic rotor-motion dynamics: The aerodynamic torque dynamics of the wind turbine is a first-order inertia, and the rotor motion equation is a second-order link:

$$G_{\mathrm{wind}}(s) = \frac{1}{1 + T_{\mathrm{wind}} s} \tag{7}$$

$$G_{\mathrm{gen}}(s) = \frac{1}{2Hs + D} \tag{8}$$

where T_{wind} is the wind turbine aerodynamic time constant, H is the rotor inertia time constant, and D is the damping coefficient.

Active power transfer function of DFIG injected into the PCC:

$$G_{\mathrm{DFIG}}(s) = G_{\text{PI-}r}(s) \cdot G_{\mathrm{Te}}(s) \cdot G_{\mathrm{gen}}(s) \cdot G_{\mathrm{wind}}(s) \tag{9}$$

2.2.3. Transfer-Function Model of Hydropower Unit

In the small-signal analysis of hydroelectric generating units, the water-hammer time constant T_w, inertia time constant H_h and damping coefficient D_h serve as the core parameters determining system stability. These parameters not only reflect the physical characteristics of the units but also fluctuate with operating conditions such as water head height and load level, acting as the primary internal cause of low-frequency oscillation at the Point of Common Coupling (PCC).

A hydropower unit involves the cascade dynamics of governor–turbine–synchronous generator, and its transfer function model is given as follows:

Governor loop: Guide vane opening regulation based on PI control:

$$G_{\mathrm{gov}}(s) = K_{\mathrm{p}-g} + \frac{K_{\mathrm{i}-g}}{s} \tag{10}$$

where $K_{\text{p-}g} = 0.7$ and $K_{\text{i-}g} = 25$ are the governor parameters.

Hydraulic turbine water-hammer effect: The transfer function of rigid water hammer (describing the dynamics from guide vane opening to hydraulic turbine output):

$$G_{\mathrm{hyd}}(s) = \frac{1 - T_w s}{1 + 0.5 T_w s} \tag{11}$$

where T_w is the water-hammer time constant (T_w= 1.2 s).

Generator rotor-motion dynamics: The electromechanical transient transfer function of the synchronous generator:

$$G_{\mathrm{syn}}(s) = \frac{1}{2H_h s + D_h} \tag{12}$$

where T_w= 1.2 s is the inertia time constant of the hydro-generator, and D_h is the damping coefficient.

Active power transfer function of hydropower unit injected into the PCC:

$$G_{\mathrm{hydro}}(s) = G_{\mathrm{gov}}(s) \cdot G_{\mathrm{hyd}}(s) \cdot G_{\mathrm{syn}}(s) \tag{13}$$

Mathematically, the rigid water-hammer model in Equation (11) is a non-minimum phase element. The parameter T_w determines the system-negative phase lead; its growth under varying operating conditions worsens phase lag, reduces damping and increases

oscillation risks. This nonlinear link is retained to reflect the hydrodynamic impact on PCC voltage stability. Equation (12) depicts the electromagnetic transients of synchronous generators, in which H_h reflects frequency disturbance sensitivity and D_h denotes oscillation damping capacity. Due to multi-power coupling and time-varying grid impedance, actual H_h and D_h are time varying. The established model offers static characterization and dynamic boundaries for robust controller design. In summary, key hydro-unit parameters greatly affect system-steady and dynamic performance. Considering significant parameter fluctuations in multi-source systems, a FOPID controller with fractional orders λ and μ is adopted to replace conventional fixed-parameter PI control. It compensates for parameter-induced model uncertainties via fractional-order properties, and enhances system robustness under wide operating conditions.

2.2.4. Transfer-Function Model of VSC-HVDC Converter Station

(1) Control System Transfer Function

The line-commutated converter (LCC)-based VSC-HVDC converter station in the system serves as a key connection unit between the PCC and the load side. It adopts a core control architecture of constant current outer loop + firing angle inner loop + Phase-Locked Loop (PLL) phase tracking. Combined with the electrical dynamic characteristics of converter transformers and converter bridges, a complete small-signal transfer function model is established as follows, laying a foundation for system-level oscillation instability analysis.

The control objective is to accurately track the reference value of active current on the grid side I_{ref} and suppress current surges caused by PCC voltage fluctuations or load mutations. The input quantity is the deviation $\Delta I = I_{\text{ref}} - I_{\text{ac}}$ between the current reference value and the actual AC-side current I_{ac}, and the output quantity is the firing angle reference value α_{ref}. The transfer function is given as

$$G_{\text{PI-lcc}}(s) = K_{\text{p-lcc}} + \frac{K_{\text{i-lcc}}}{s} \tag{14}$$

where $K_{\text{p-lcc}}$ is the proportional gain (based on the 5000 MVA rated capacity of the LCC, set to 0.8), which is used to improve the current response speed, and $K_{\text{i-lcc}}$ is the integral gain (set to 35 in this paper), which is adopted to eliminate steady-state current errors. The coordination of the two gains is required to avoid control overshoot and oscillation.

PLL Phase-Tracking Loop: The LCC relies on the grid-commutated mechanism and requires the PLL to track the PCC bus voltage phase in real time, providing a synchronous reference for precise firing-angle control. Considering the dynamic response characteristics of PLL, it is approximated as a second-order damped oscillation link under small-signal conditions, with its transfer function expressed as

$$G_{\text{PLL}}(s) = \frac{K_{\text{p-pll}}s + K_{\text{i-pll}}}{s^2 + K_{\text{p-pll}}s + K_{\text{i-pll}}} \tag{15}$$

where $K_{\text{p-pll}}$ is the PLL proportional gain (set to 15 in this paper) and $K_{\text{i-pll}}$ is the PLL integral gain (set to 80 in this paper); the damping ratio of the second-order system is expressed as $\zeta = K_{\text{p-pll}}/(2\sqrt{K_{\text{i-pll}}})$. This is designed as $\zeta = 0.707$ (critical damping) in this paper, so as to avoid commutation inaccuracy caused by phase-tracking delay.

Firing-Angle Dynamic Loop: The generation of firing pulses, conduction delay of power devices and sampling lag of control hardware lead to a dynamic delay from the reference firing angle to the actual one. It is approximated as a first-order inertial link under small-signal conditions:

$$G_{\alpha}(s) = \frac{1}{1 + T_{\alpha}s} \tag{16}$$

where T_α is the firing-angle response-time constant (set to 0.02 s in this paper), which directly affects the dynamic response speed of LCC current regulation.

(2) Transfer Function of Electrical Main Circuit

A 12-pulse converter bridge topology (2 sets of 6-pulse converter bridges connected in series) is adopted, whose core function is to realize AC/DC energy conversion via the regulation of firing angle α. Under small-signal conditions, minor fluctuations in the commutation overlap angle γ are ignored (when $\gamma \leq 15^\circ$, its impact is negligible), and the dynamic relationship between the firing angle of the converter bridge and the injected current on the AC side is approximated as the proportional link

$$G_{\text{bridge}}(s) = K_{\text{bridge}} \tag{17}$$

where K_{bridge} is the proportional coefficient, determined by the system's electrical parameters, with the calculation formula

$$K_{\text{bridge}} = \frac{\sqrt{6}U_{\text{ac}}}{2X_t} \tag{18}$$

where U_{ac} is the rated line voltage of the PCC bus (500 kV) and X_t is the leakage reactance of the converter transformer (set to 0.12 pu in this paper). Substituting the parameters gives $K_{\text{bridge}} \approx 1800$ A/rad.

The converter transformer is used to isolate the AC and DC systems and regulate the commutation voltage level, and its leakage reactance is a key parameter affecting commutation characteristics. Under small-signal conditions, the electromagnetic transient response speed of the transformer is much faster than that of the control loop, so it can be approximated as a pure reactance link, with the transfer function

$$G_{\text{trans}}(s) = \frac{1}{sL_t} \tag{19}$$

where the leakage inductance L_t of the converter transformer is converted from the per-unit value of leakage reactance:

$$L_t = \frac{X_t U_{\text{ac}}^2}{S_{\text{rated}} \cdot 2\pi f_N} \tag{20}$$

where S_{rated} is the rated capacity of the LCC (5000 MVA) and f_N is the rated frequency of the power grid (50 Hz). Substituting the parameters gives $L_t \approx 0.087H$.

(3) Overall Transfer Function of LCC Injected into the PCC

The complete dynamic process of the LCC converter station (from the current reference value to the current injected into the PCC) consists of the series connection of each link, and the overall transfer function is integrated as follows:

$$G_{\text{LCC}}(s) = G_{\text{PI-lcc}}(s) \cdot G_{\text{PLL}}(s) \cdot G_\alpha(s) \cdot G_{\text{bridge}}(s) \cdot G_{\text{trans}}(s) \tag{21}$$

Substituting the specific expressions of each link, the expanded form is

$$G_{\text{LCC}}(s) = \left(K_{\text{p-lcc}} + \frac{K_{\text{i-lcc}}}{s}\right) \cdot \frac{K_{\text{p-pll}}s + K_{\text{i-pll}}}{s^2 + K_{\text{p-pll}}s + K_{\text{i-pll}}} \cdot \frac{1}{1 + T_\alpha s} \cdot K_{\text{bridge}} \cdot \frac{1}{sL_t} \tag{22}$$

3. Fractional-Order PI/FOPID Controllers

3.1. Background and Core Objectives

In hydro–wind–photovoltaic hybrid systems, the random output fluctuations of photovoltaic and wind power generation, the nonlinear characteristics of the water-hammer effect in hydropower units, and the oscillation instability caused by multi-source power coupling at the PCC impose stringent requirements on the dynamic response speed, robustness and steady-state accuracy of control strategies. Traditional integer-order PI controllers only rely on proportional-gain K_p and integral-gain K_i for regulation, which cannot adapt to the complex nonlinear dynamics and wide operating condition fluctuations of the system, and are prone to problems such as large overshoot, insufficient oscillation suppression and performance degradation under parameter perturbations. Based on fractional-order calculus theory, this section presents the design of two types of controllers, namely fractional-order PI (FOPI) and fractional-order PID (FOPID). By expanding the degrees of freedom of control orders, the adaptability to complex system dynamics and oscillation-suppression effects are enhanced, laying a theoretical foundation for subsequent parameter optimization combined with the CMOPSO algorithm.

3.2. Fundamentals of Fractional-Order Calculus

Fractional-order calculus is a generalized extension of integer-order calculus. Its core advantage lies in allowing integral and differential orders to take arbitrary non-integer real values, which can more accurately characterize the dynamic behaviors of complex systems with memory and nonlinearity. In the engineering field, the definition of fractional-order operators mostly adopts the Caputo form, whose mathematical expression is given as follows:

3.2.1. Caputo Fractional-Order Integral Operator

For the continuous-time function $e(t)$, its Caputo fractional-order integral operator $D^{-\lambda}[\cdot]$ (with integral order $\lambda > 0$) is defined as [25]

$$D^{-\lambda}e(t) = \frac{1}{\Gamma(\lambda)}\int_0^t (t-\tau)^{\lambda-1}e(\tau)d\tau \tag{23}$$

where $\Gamma(\cdot)$ is the Gamma function, which describes the memory characteristic of fractional-order integration, i.e., the current control action depends on all historical information regarding the error signal, with weights decaying over time.

3.2.2. Caputo Fractional-Order Differential Operator

For the continuous-time function e(t), its Caputo fractional-order differential operator $D^{\mu}[\cdot]$ (with differential order $0 < \mu < 1$) is defined as

$$D^{\mu}e(t) = \frac{1}{\Gamma(1-\mu)}\int_0^t (t-\tau)^{-\mu}\dot{e}(\tau)d\tau \tag{24}$$

This operator can flexibly adjust the frequency response characteristics of the system through non-integer-order differential operations, providing additional degrees of freedom for controller design.

3.3. FOPI Controller

The FOPI controller is a fractional-order extension of the traditional integer-order PI controller [26]. It retains the core links of proportional (P) and integral (I), and extends

the integral order from the fixed integer 1 to a real number within 0–1, Both λ and μ are constrained in the range of 0 to 1. Its control law expression is

$$u_{\mathrm{FOPI}}(t) = K_p e(t) + K_i D^{-\lambda} e(t) \tag{25}$$

where $u_{\mathrm{FOPI}}(t)$ is the output-control quantity of the FOPI controller; $\mathrm{e(t)} = \mathrm{r(t)} - \mathrm{y(t)}$ is the system error signal; r(t) is the reference input (e.g., rated voltage of PCC); y(t) is the actual system output; K_p is the proportional gain, which is used to quickly respond to the error signal and improve the dynamic response speed of the system; K_i is the integral gain, which is adopted to eliminate steady-state errors and enhance the steady-state accuracy of the system; and $\lambda \in (0, 2]$ is the fractional-order integral order, and adjusting this parameter can continuously optimize the memory characteristic of the integral link to adapt to the nonlinear dynamics of the system.

By performing the Laplace transform on the control law, the transfer function of the FOPI controller is obtained as

$$G_{\mathrm{FOPI}}(s) = \frac{U_{\mathrm{FOPI}}(s)}{E(s)} = K_p + \frac{K_i}{s^{\lambda}} \tag{26}$$

3.4. FOPID Controller

To further enhance the suppression capability for PCC oscillations, a fractional-order differential link is introduced on the basis of the FOPI controller to construct the FOPID controller [27]. By adding the differential gain K_d and fractional-order differential order μ, this controller increases two control degrees of freedom, enabling more precise suppression of transient disturbances and oscillation attenuation. Its control law expression is

$$u_{\mathrm{FOPID}}(t) = K_p e(t) + K_i D^{-\lambda} e(t) + K_d D^{\mu} e(t) \tag{27}$$

where $u_{\mathrm{FOPID}}(t)$ is the output control quantity of the FOPID controller; $K_d \in (0, 1]$ is the differential gain, which is used to predict the variation trend of the error signal and suppress system overshoot and oscillations; and $\mu \in (0, 1]$ is the fractional-order differential order, and continuously adjusting this parameter can optimize the disturbance response characteristic of the differential link, avoiding the noise sensitivity issue of the integer-order differential link.

By performing the Laplace transform on the control law, the transfer function of the FOPID controller is obtained as

$$G_{\mathrm{FOPID}}(s) = \frac{U_{\mathrm{FOPID}}(s)}{E(s)} = K_p + \frac{K_i}{s^{\lambda}} + K_d s^{\mu} \tag{28}$$

when $\lambda = 1$ and $\mu = 1$ this transfer function degrades into the traditional integer-order PID controller, which verifies the universality and expansibility of the FOPID controller.

The structure diagram of the Fractional-Order PID Controller is as shown in Figure 2:

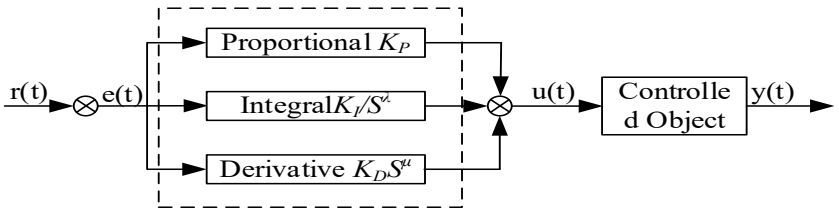


Figure 2. Structure of the Fractional-Order PID Controller.

3.5. Controller-System Adaptability

The hydro–wind–photovoltaic grid-connected system exhibits characteristics of nonlinearity, time-varying nature, and multi-disturbance coupling. Traditional integer-order controllers, due to limited parameter degrees of freedom, struggle to achieve an optimal balance among oscillation suppression, steady-state accuracy, and dynamic response [28].

The FOPI and FOPID controllers demonstrate stronger system adaptability through flexible adjustment of fractional orders [29]:

For the randomness of wind and photovoltaic power fluctuations, the fractional-order integral link can adjust memory weights via λ to balance the error accumulation speed and disturbance adaptability;

For low-frequency oscillations caused by the water-hammer effect, the fractional-order differential link of the FOPID controller can precisely match the oscillation frequency via μ, enhancing damping characteristics and quickly attenuating the oscillation amplitude;

The multi-parameter regulation system of these two controllers is highly compatible with the multi-objective optimization capability of the CMOPSO algorithm, and the control objective of "optimal PCC voltage-tracking accuracy + minimal oscillation instability risk" can be achieved through cooperative optimization.

4. Multi-Objective Optimization Method

4.1. Problem Description

In the hydro–wind–photovoltaic hybrid grid-connected system, the voltage at the PCC is prone to low-frequency oscillations under disturbances [30]. Excessively large oscillation amplitude or insufficient damping may lead to oscillation amplification and even instability. Therefore, it is necessary to optimize the control parameters to improve the dynamic performance of the system while effectively reducing the risk of PCC oscillation instability. To this end, this paper introduces the Deep Reinforcement Learning-assisted Surrogate-Assisted Evolutionary Algorithm (DRL-SAEA), takes the PCC voltage dynamic response as the optimization object, and constructs a multi-objective optimization framework with ITAE and ODRI as the dual objectives.

4.2. Objective Functions

4.2.1. ITAE Index

To evaluate the overall performance of the PCC voltage dynamic response, the ITAE is adopted as the first optimization objective, which is defined as

$$J_1 = \text{ITAE} = \int_{t_0}^{t_f} t \cdot \left| V_{\text{PCC}}(t) - V_{\text{ss}} \right| dt \tag{29}$$

where J_1 ($V \cdot s^2$) is the ITAE performance index; $V_{\text{PCC}}(t)$ is the PCC voltage amplitude at time t (p.u.); V_{ss} is the steady-state value of PCC voltage (p.u.); t is the time variable (s); t_0 is the disturbance occurrence time (s); and t_f is the evaluation termination time (s).

The ITAE index assigns higher weights to late-stage errors, which can effectively reflect the oscillation attenuation speed and steady-state recovery capability of the system.

4.2.2. Oscillation Disturbance Risk Index

To further characterize the potential instability risk caused by PCC voltage oscillations, this paper proposes an ODRI, whose mathematical expression is

$$J_2 = \text{ODRI} = \frac{\int_{t_0}^{t_f} (V_{\text{PCC}}(t) - V_{\text{ss}})^2 dt}{\delta} \tag{30}$$

where J_2 ($V^2 \cdot s$) is the ODRI and δ is the oscillation logarithmic decrement, which is used to characterize the damping capability of the system.

The calculation method of the oscillation logarithmic decrement δ is

$$\delta = \ln\left(\frac{A_1}{A_2}\right) \tag{31}$$

where A_1 is the amplitude of the first oscillation peak relative to the steady-state value in the PCC voltage response and A_2 is the amplitude of the next oscillation peak with the same polarity as A_1.

The numerator term of ODRI reflects the cumulative effect of oscillation energy in the time domain, while the denominator term reflects the damping dissipation capability of the system. When the oscillation amplitude is large and the damping is insufficient, the value of ODRI will increase significantly, indicating that the system has a high risk of oscillation instability.

4.3. Overview of CMOPSO Algorithm

The CMOPSO is an intelligent optimization algorithm, improved based on the multi-population co-evolution mechanism, specifically designed to solve multi-objective optimization problems (MOPs). This algorithm breaks through the limitations of traditional single-population optimization: through the multi-population division of labor, collaboration, and information sharing mechanism, it enhances diversity while ensuring the convergence of the solution set. It is particularly suitable for complex optimization scenarios in power systems (such as PCC voltage oscillation suppression) that involve multi-objective conflicts (e.g., dynamic response speed vs. steady-state accuracy, oscillation suppression vs. robustness).

4.4. Algorithm Flow

To meet the multi-objective optimization requirements for PCC voltage oscillation suppression, the implementation flow of the CMOPSO algorithm is as follows:

Definition of Optimization Objectives: Take the control parameters of the turbine governor system as optimization variables, and establish a dual-objective optimization model for ITAE and ODRI.

Population Initialization: Two sub-populations are constructed corresponding to the two optimization objectives (ITAE and ODRI), each with a population size of 50 (total population: N = 100). This configuration ensures sufficient search density for each objective while balancing convergence speed, computational efficiency, and the diversity of the Pareto-optimal frontier. The search ranges of control parameters are determined according to engineering practice and extensive pre-simulation tests.

Fitness Evaluation: Each population calculates fitness based on the corresponding objective function, to avoid interference from multi-objective conflicts.

Archiving and Updating: After each generation of iteration, all non-dominated solutions are stored in an external archive. The optimal solution set is screened via crowding distance to ensure the uniformity of solutions.

Termination Condition: Stop the search when the number of iterations reaches 5000 generations or the archived solution set tends to be stable, and output the compromise solution from the Pareto-optimal solution set as the control parameter.

Compared with traditional optimization algorithms, the core advantages of CMOPSO are: ① Multi-population division of labor and collaboration enables more efficient resolution of multi-objective conflict issues; ② The external archiving mechanism ensures the convergence and diversity of the solution set, avoiding premature convergence; ③ The

update strategy integrating elite solutions improves the accuracy and robustness of parameter optimization for complex systems, which exactly matches the characteristics of the turbine governor system (nonlinearity, large inertia and strong coupling) and can effectively optimize the PCC voltage oscillation-suppression effect.

The algorithm flow chart is shown in Figure 3.

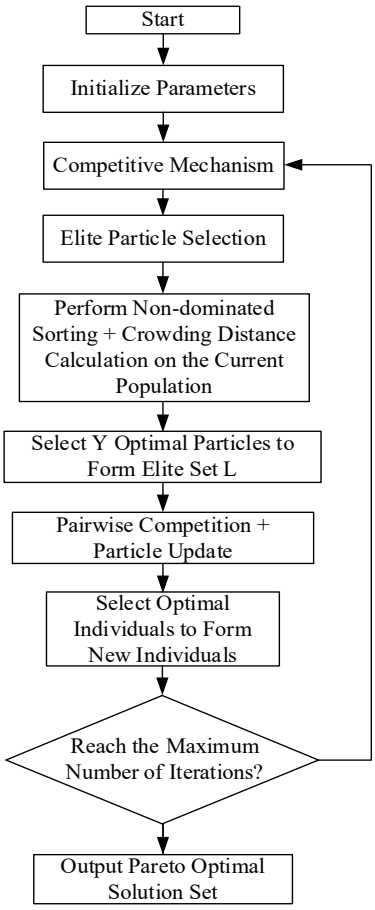


Figure 3. CMOPSO algorithm flow chart.

4.5. Method Advantages

Compared with traditional single-objective or empirical parameter-tuning methods, the method proposed in this paper has the following advantages: it simultaneously takes into account dynamic performance and oscillation instability risk; realizes quantitative evaluation of oscillation risk via the ODRI index; and is applicable to complex grid-connected systems dominated by power electronics.

5. Simulation and Result Analysis

5.1. Simulation Model Architecture

Based on the topology of the hydro–wind–photovoltaic hybrid system with VSC-HVDC transmission (Figure 1), a complete simulation model is built in Simulink (R2024b, MathWorks, Natick, MA, USA), focusing on the control parameter optimization of the turbine governor system and comparative analysis of the control performances of FOPI and FOPID controllers. The hydraulic turbine adopts a cascaded model of "governor–controller–water hammer effect–generator". The optimization objects are the core parameters of the two types of controllers:

FOPI controller: adopts a three-parameter regulation system consisting of proportional gain K_p, integral gain K_i and fractional-order integral order λ.

FOPID controller: adds a differential link on the basis of FOPI, forming a five-parameter regulation system including proportional gain K_p, integral gain K_i, differential gain K_d, fractional-order integral order λ and fractional-order differential order μ. The differential link enhances the system's response speed to instantaneous disturbances and improves oscillation-suppression capability.

The Model Framework Diagram is shown in Figure 4.

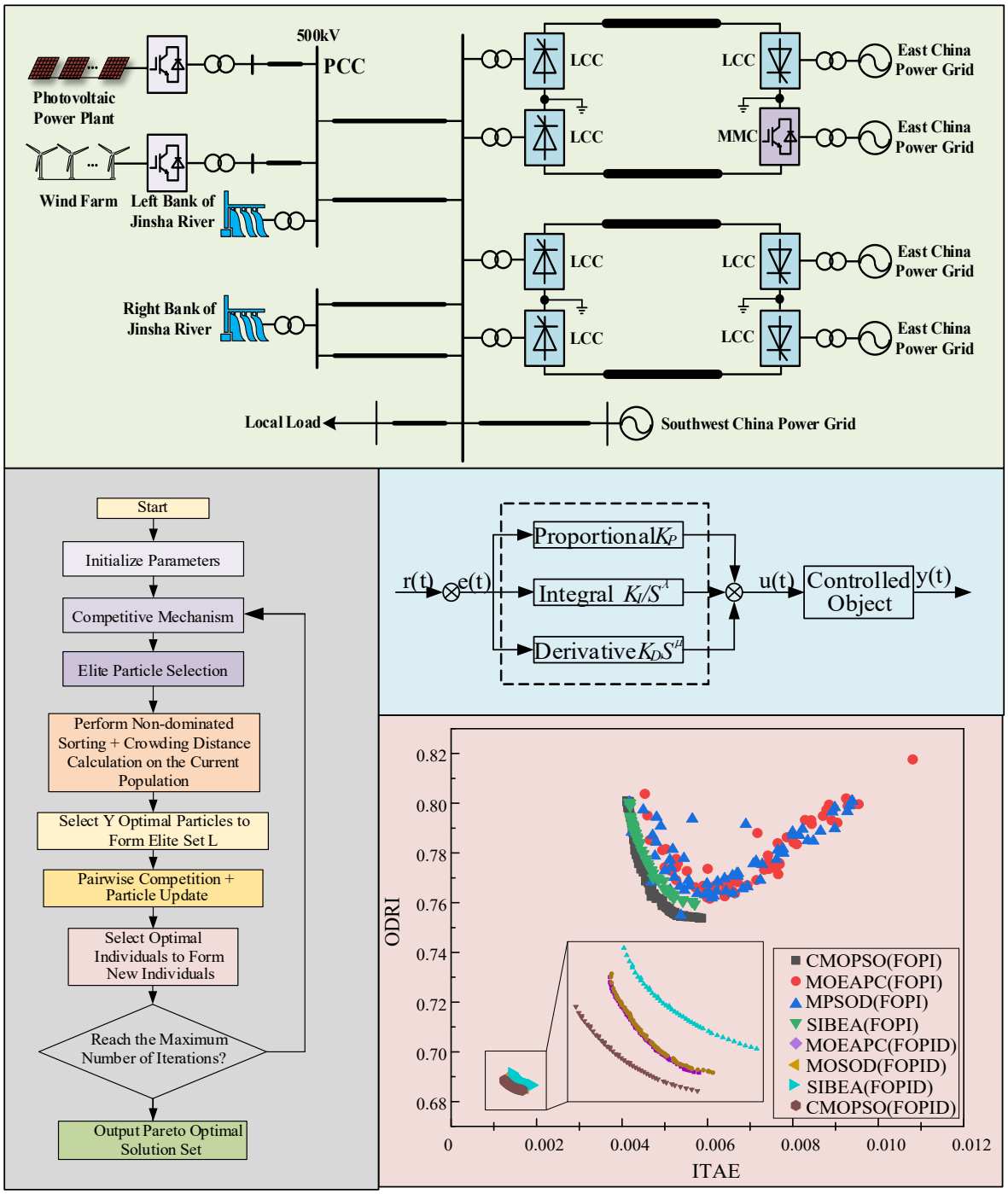


Figure 4. Model framework diagram.

5.2. Optimization Algorithm and Experimental Design

With the objectives of optimal PCC voltage dynamic response performance and minimal oscillation instability risk, the experiment adopts four multi-objective optimization

algorithms (CMOPSO, MPSOD, SIBEA, and MOEAPC) to optimize the parameters of FOPI and FOPID controllers. The algorithm parameter configuration uniformly follows the PlatEMO experimental standards: population size N = 100, and maximum number of evaluations maxFE = 10,000. Specifically, for CMOPSO and MPSOD, the inertia weight **w** is set to 0.4 and the learning factors c_1, c_2 are both 1.5; for SIBEA, the crossover and mutation probabilities are $P_c = 0.9$ and $P_m = 0.1$; for MOEAPC, the reference point scale H is 10. Under identical computing environments, the average computational times for CMOPSO, MPSOD, SIBEA, and MOEAPC are approximately 156 s, 142 s, 185 s, and 168 s, respectively. The variable ranges are determined by engineering experience and simulation tests. Pareto frontiers corresponding to the two controllers are generated via optimization for comparative analysis of their performances; meanwhile, the optimal optimization algorithm for each controller is selected based on frontier distribution and performance indicators.

Figure 5 shows the comparison diagram of multi-objective Pareto frontiers of FOPI and FOPID controllers under the four algorithms. The horizontal axis represents the ITAE index (characterizing PCC voltage tracking accuracy, with smaller values being better), and the vertical axis represents the ODRI index (characterizing system oscillation instability risk, with smaller values being better).

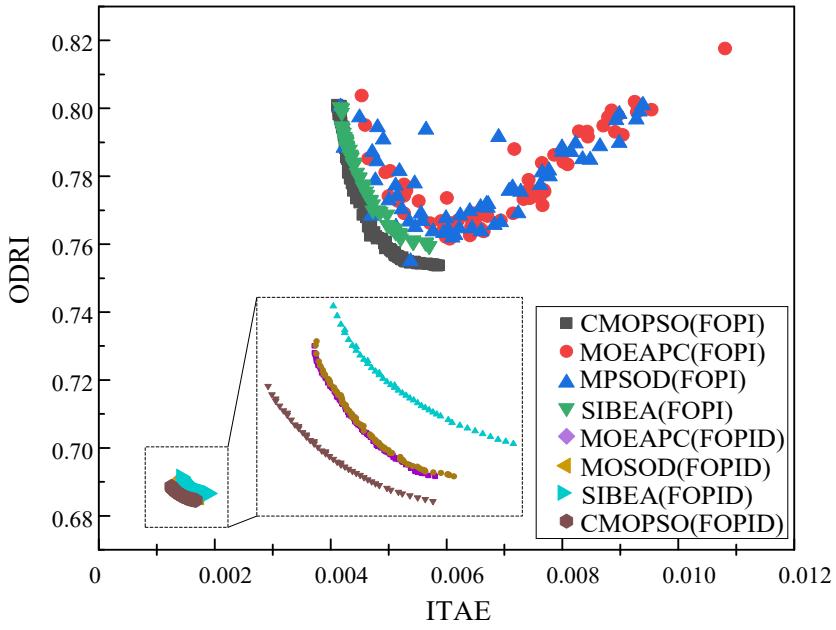


Figure 5. Comparison diagram of multi-objective Pareto frontiers.

As shown in Figure 5, the Pareto fronts generated by optimizing the FOPI controller using the MOEAPC and MPSOD algorithms have significant flaws: the solution sets contain a large number of dominated solutions (i.e., there exist other solutions that are superior in both the ITAE and ODRI objectives) and fail to effectively approach the Pareto-optimal region. In contrast, the Pareto front of the FOPID controller is generally closer to the coordinate origin, with non-dominated solutions being of higher quality. It is comprehensively superior to the FOPI controller in both voltage-tracking accuracy and oscillation-suppression capability, highlighting the superiority of its control structure.

On the basis of confirming that the FOPID controller outperforms the FOPI controller, we further focus on the FOPID controller to analyze the impact of different optimization algorithms on its dual-objective coordinated optimization performance, and the results are shown in Figure 6.

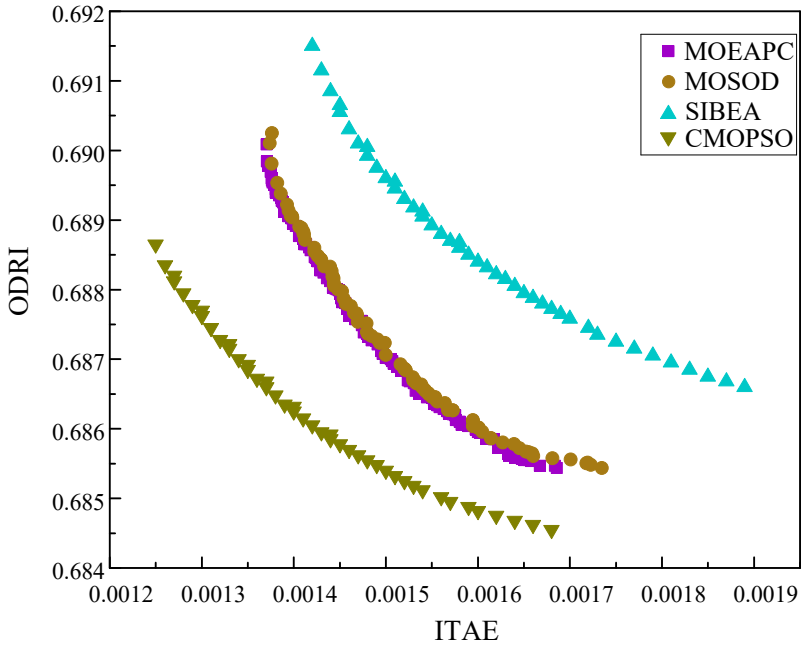


Figure 6. Pareto frontiers of FOPID controller optimized by different algorithms.

It can be seen from Figure 6 that the Pareto frontier corresponding to the CMOPSO algorithm is entirely located in the lower-left area of the objective space. The ITAE and ODRI indices of its non-dominated solutions are significantly superior to those of the other three algorithms, with continuous and uniform solution distribution, which fully demonstrates the algorithm's advantages of strong convergence and solution diversity in dual-objective coordinated optimization. The Pareto frontier of the SIBEA algorithm is entirely skewed to the upper-right area, with core performance indices inferior to CMOPSO and limited solution coverage. The Pareto solutions for the MPSOD algorithm are relatively scattered, with invalid solutions that cause unbalanced trade-off between objectives, leading to insufficient balance in dual-objective optimization. The Pareto frontier of the MOEAPC algorithm is located in the area closest to the upper-right, showing not only the worst key performance indices but also sparse and discrete solution distribution, thus presenting the weakest optimization performance among the four algorithms. The comparison results verify the adaptability and superiority of the CMOPSO algorithm for FOPID controller parameter optimization; its generated Pareto frontier is closer to the ideal point of dual-objective optimization, which can provide more practically valuable optimal parameter combinations for engineering practice.

The compromise solutions for the Pareto frontier under each controller (balancing the optimal trade-off between ITAE and ODRI) are selected, and the corresponding control parameters are shown in Table 1. Among them, the differential gain (K_d) and fractional-order differential order (μ) of the FOPID controller are adapted to the system dynamic characteristics through optimization, achieving precise suppression of the water-hammer effect and wind–photovoltaic fluctuations.

The comparison diagram of PCC voltage amplitude drawn with the optimized FOPID parameters is shown as follows:

It can be seen from Figure 7 that in the initial disturbance stage, some curves show large overshoot and more drastic voltage fluctuations; in the oscillation stage, the curves optimized by high-performance algorithms feature small oscillations and fast attenuation, suppressing fluctuations rapidly, while those optimized by inferior algorithms suffer from prolonged oscillations and slow attenuation; in the steady-state stage, the curves of high-performance algorithms stably converge to 1 p.u., whereas slight residual fluctuations

remain in some curves. Parameters optimized by CMOPSO precisely match the characteristics of the governor system, achieving "small fluctuation and fast recovery" of the PCC voltage; parameters of inferior algorithms fail to balance dynamic response and stability, resulting in poor regulation performance. Parameters from high-performance algorithms ensure grid-voltage stability, while those from inferior ones aggravate fluctuations and increase the risk of instability.

Table 1. Control parameters of hydro-turbine units optimized by different algorithms.

Controller	Optimization Algorithm	K_{p1}	K_{i1}	λ_1	K_{d1}	μ_1	K_{p2}	K_{i2}	λ_2	K_{d2}	μ_2
FOPI	CMOPSO	59.95	0.35	0.67	-	-	0.42	51.32	0.58	-	-
FOPI	MPSOD	13.93	0.84	0.52	-	-	0.11	32.64	0.61	-	-
FOPI	SIBEA	19.28	0.82	0.59	-	-	0.59	26.73	0.66	-	-
FOPI	MOEAPC	45.00	0.42	0.71	-	-	0.14	10.66	0.74	-	-
FOPID	CMOPSO	62.31	0.32	0.71	0.08	0.35	0.45	53.68	0.62	0.07	0.29
FOPID	MPSOD	16.42	0.79	0.56	0.05	0.41	0.13	34.21	0.64	0.04	0.37
FOPID	SIBEA	22.51	0.78	0.63	0.06	0.38	0.62	28.35	0.69	0.05	0.33
FOPID	MOEAPC	48.73	0.39	0.75	0.04	0.43	0.16	12.41	0.78	0.03	0.39

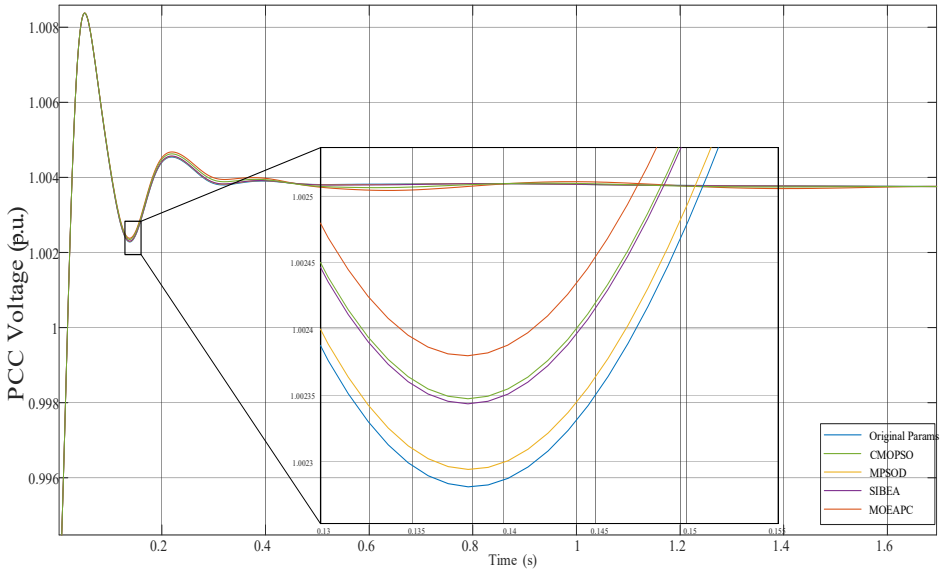


Figure 7. PCC voltage-response comparisons under different algorithms.

Combined with the PCC voltage-response performance indicators in Table 2, it can be concluded that with ITAE and ODRI as the dual optimization objectives, the proposed CMOPSO algorithm exhibits significantly better performance than the original parameters and other comparative algorithms (MPSOD, SIBEA, and MOEAPC). Specifically, the ITAE index of CMOPSO (0.00132) is the smallest among all schemes, representing a 12.58% reduction compared with the original parameters (0.00151), which demonstrates superior steady-state voltage-tracking accuracy. Its ODRI index (0.670) is also the best among all groups, decreasing by 2.47% versus the original parameters (0.687), verifying the algorithm's stronger capability to suppress oscillation disturbance risks. Among the comparative algorithms, although both indices of MPSOD, SIBEA and MOEAPC are better than the original parameters, none of them achieve the dual-objective coordinated optimization effect as CMOPSO does. The above results indicate that the CMOPSO algorithm can more effectively balance the core requirements of "steady-state accuracy" and "anti-oscillation stability" of PCC voltage in hydro–wind–photovoltaic grid-connected systems, making it a more suitable controller-parameter optimization method for this scenario.

Table 2. PCC voltage-response performance indicators under different algorithms.

	Original Params	CMOPSO	MPSOD	SIBEA	MOEAPC
ITAE	0.00151	0.00132	0.00144	0.00147	0.00150
ODRI	0.687	0.670	0.688	0.681	0.683

The DC bus is the core link for power transmission and energy buffering in the hydro–wind–photovoltaic hybrid system. Its voltage stability directly determines the continuity of power distribution and the operational safety of converter equipment. Therefore, we further analyze the dynamic response characteristics of the Vdc after optimizing the FOPID controller with different algorithms, and the results are shown in Figure 8.

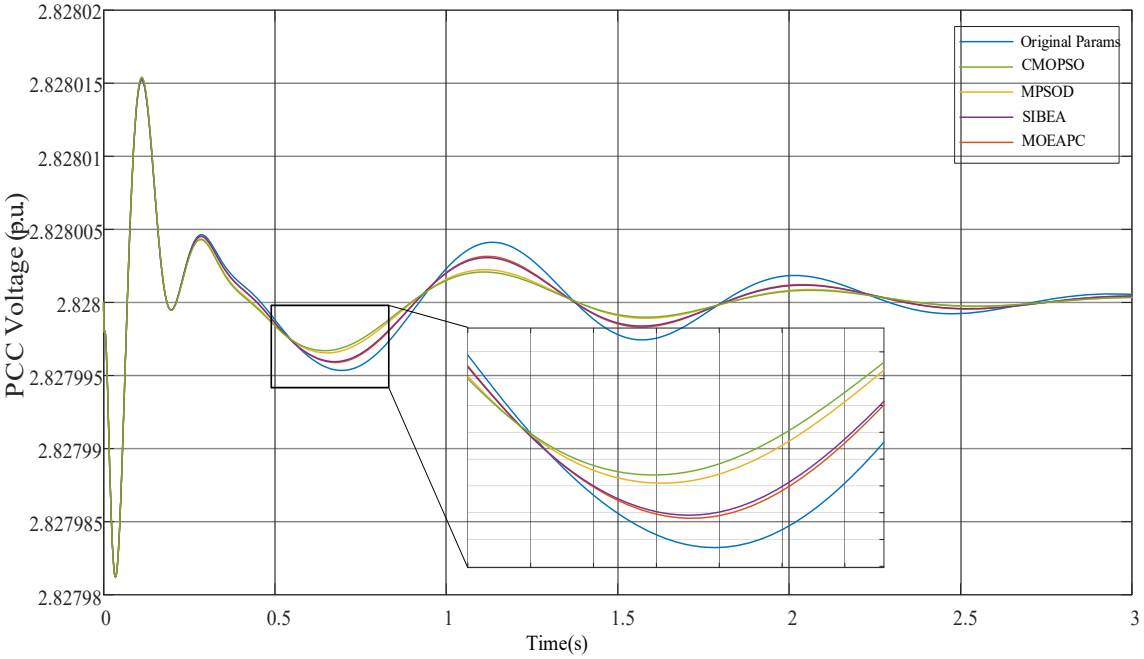


Figure 8. Comparison of dynamic-response waveforms of Vdc under different parameters.

The different curves in Figure 8 correspond to the voltage response waveforms of the FOPID controller optimized by the original parameters and the four algorithms (CMOPSO, MPSOD, SIBEA, and MOEAPC). As can be seen from the Figure 8, the DC bus voltage corresponding to the original parameters shows significant overshoot, large fluctuation amplitude and a slow convergence process after disturbance. After the parameter optimization of the FOPID controller, the voltage response of all algorithms is improved, with the waveform optimized by the CMOPSO algorithm performing the best: it has the smallest overshoot in the initial disturbance stage, the voltage fluctuation amplitude during the dynamic process is significantly lower than that of other algorithms, and it can quickly converge to the steady-state value without residual fluctuations in the later stage, which fully demonstrates the control flexibility of the FOPID controller and the optimization adaptability of the CMOPSO algorithm.

To quantitatively verify the conclusions regarding the above waveform analysis, the ITAE (voltage-tracking accuracy) and ODRI (oscillation instability risk) indices of the DC bus voltage under different parameters are calculated, and the results are shown in Table 3.

Table 3. Performance indicators of Vdc under different parameters.

	Original Params	CMOPSO	MPSOD	SIBEA	MOEAPC
ITAE	0.088763	0.029922	0.035601	0.044132	0.046531
ODRI	0.001954	0.001266	0.001362	0.000881	0.000824

Table 3 presents the core performance indicators corresponding to the unoptimized original parameters and the FOPID controller parameters optimized by the four algorithms (CMOPSO, MPSOD, SIBEA, and MOEAPC). The data shows that both the ITAE (0.088763) and ODRI (0.001954) of the original parameters are the largest among all groups, indicating the worst voltage-tracking accuracy and the highest risk of oscillation instability. By contrast, the FOPID controller parameters optimized by the four algorithms all achieve improved indicators, among which those optimized by the CMOPSO algorithm perform the best. Its ITAE (0.029922) is the smallest across all combinations; although its ODRI (0.001266) is slightly higher than that of SIBEA and MOEAPC, it achieves the optimal balance between voltage-tracking accuracy and oscillation-suppression capability in line with the dual-objective coordinated optimization requirements. This fully verifies the optimization adaptability of the CMOPSO algorithm for FOPID controller parameters, as well as the remarkable advantages of this combined strategy in improving DC bus voltage stability.

5.3. Performance Evaluation of Optimized Parameters with Upss and Qe_sum Waveforms

Dynamic response waveforms are intuitive carriers reflecting the regulation performance of control parameters; their characteristics such as overshoot, response time and steady-state fluctuation directly correspond to system stability and control accuracy. To further compare the parameter performance of different optimization algorithms, this section takes the key control signals of the hydro–wind–photovoltaic grid-connected system as the research object, and displays the waveform differences of the CMOPSO algorithm, MPSOD, SIBEA, and MOEAPC algorithms and the original parameter group under disturbance conditions: first, the supplementary excitation-control signal Upss of the hydro-generator excitation system, which reflects the low-frequency oscillation-suppression capability; second, the total reactive power output of photovoltaic inverters Qe_sum, which reflects the reactive power support response characteristic. Through the comparison of the two types of waveforms, combined with quantitative indicators such as response time, overshoot and steady-state error, the regulation effect of each optimized parameter is systematically evaluated, verifying the prominent advantages of the CMOPSO algorithm in dual-objective coordinated optimization.

Figure 9 presents the dynamic response comparison of the supplementary excitation control signal (Upss) of the hydro-generator excitation system under parameters optimized by different algorithms. The horizontal axis represents time (s) and the vertical axis denotes the amplitude of the Upss signal (magnitude $\times 10^{-4}$). As the core output of the Power System Stabilizer (PSS), the fluctuation characteristics of this signal directly reflect the system's low-frequency oscillation-suppression capability.

It can be seen from the waveforms that the Upss signal of the original parameter group fluctuates most drastically (with an initial peak value close to 7×10^{-4}) and features slow oscillation attenuation, indicating that unoptimized parameters cannot effectively suppress system oscillations; although the signal-fluctuation amplitudes of the MOEAPC, SIBEA and MPSOD groups are reduced to some extent, sustained oscillations still exist with slow convergence speed; and the Upss signal of the CMOPSO group converges to the steady-state value rapidly, with the smallest fluctuation amplitude and no subsequent oscillations, which

clearly demonstrates the optimal suppression effect of CMOPSO-optimized parameters on low-frequency oscillations of the hydro-generator excitation system.

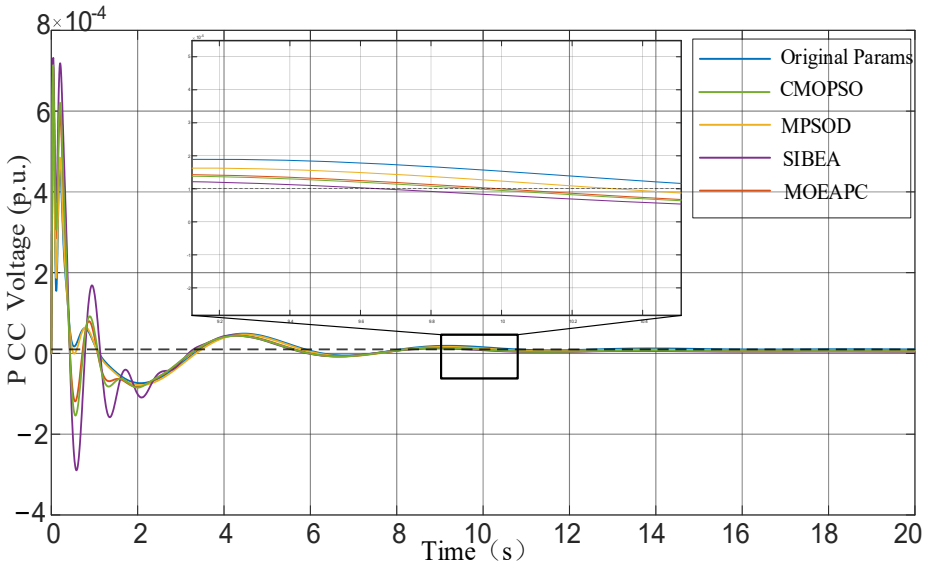


Figure 9. Comparison diagram of supplementary excitation control signals of hydro-generator excitation system.

Table 4 quantifies the ITAE and ODRI performance of the Upss signal under different parameters, where a smaller ITAE indicates higher accuracy of the signal tracking the steady-state value, and a smaller ODRI indicates lower oscillation risk. The data shows that the ITAE of the CMOPSO group (0.00092043) is significantly lower than that of the original parameter group (0.00096343), as well as the MPSOD, SIBEA and MOEAPC groups, demonstrating that its Upss signal has the best steady-state tracking accuracy. Meanwhile, the ODRI of the CMOPSO group (0.42679) is only higher than that of the original parameter group and is superior to those of the SIBEA and MOEAPC groups. Combined with the waveform characteristics in Figure 10, it can be concluded that the CMOPSO algorithm achieves a dual-objective balance of high-precision tracking and low oscillation risk while ensuring the fast convergence of the Upss signal, verifying that its optimized parameters have better comprehensive regulation performance.

Table 4. Performance indicators of Upss under different parameters.

	Original Params	CMOPSO	MPSOD	SIBEA	MOEAPC
ITAE	0.00096343	0.00092043	0.00096065	0.00096137	0.00091972
ODRI	0.36902	0.42679	0.38002	0.54298	0.4455

Figure 10 shows the dynamic response comparison of the total reactive power output of photovoltaic inverters under parameters optimized by different algorithms. The horizontal axis represents time (s) and the vertical axis denotes the per-unit value of reactive power (the base value corresponds to the rated reactive capacity of the system). This waveform reflects the reactive power support response capability of photovoltaic inverters to PCC voltage fluctuations: the reactive power of the original parameter group fluctuates most significantly (with the largest deviation from the steady-state value in the initial stage) and has a slow convergence speed; the fluctuation amplitudes of the MPSOD, SIBEA and MOEAPC groups are reduced to some extent but still have slight oscillations; while the reactive power of the CMOPSO group converges to the steady-state value more rapidly, with the smallest fluctuation amplitude and no subsequent oscillations. This intuitively in-

dicates that the CMOPSO-optimized parameters enable photovoltaic inverters to respond to voltage disturbances more accurately and rapidly, providing stable reactive power support.

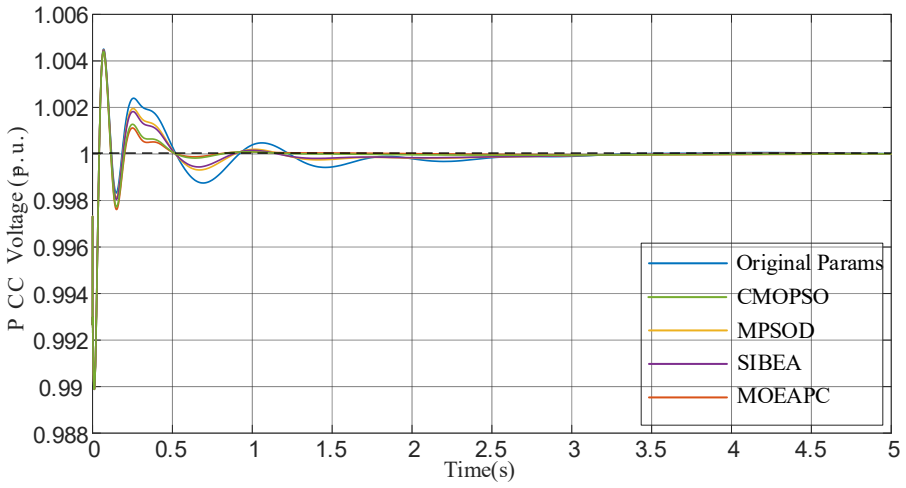


Figure 10. Comparison diagram of total reactive power output waveforms of photovoltaic inverters.

Table 5 quantifies the ITAE and ODRI indicators of the total reactive power of photovoltaic inverters under different parameters, where a smaller ITAE indicates higher reactive power-tracking accuracy and a smaller ODRI indicates lower oscillation risk. The data shows that the ITAE of the CMOPSO group (0.0003339) is far lower than that of the original parameter group (0.0016543) and other comparative algorithm groups, demonstrating the superior steady-state tracking accuracy of reactive power. Its ODRI (0.89975) is also significantly lower than that of the original parameter group (2.0097) and only slightly higher than that of the MOEAPC group. Combined with the waveform characteristics in Figure 7, it can be concluded that the CMOPSO algorithm achieves coordinated optimization of high-precision tracking and low oscillation risk while ensuring fast response of reactive power, verifying the comprehensive performance advantages of its parameters in reactive power regulation of photovoltaic inverters.

Table 5. Performance indicators of total reactive power output of photovoltaic inverters under different parameters.

	Original Params	**CMOPSO**	**MPSOD**	**SIBEA**	**MOEAPC**
ITAE	0.0016543	0.0003339	0.0010899	0.00095819	0.00040391
ODRI	2.0097	0.89975	1.5039	1.3853	0.94409

5.4. Robustness and Disturbance Analysis

While this study focuses on small-signal stability and dynamic regulation, the robustness of the FOPID-CMOPSO strategy is inherently verified through two aspects. First, the simulation includes stochastic power fluctuations from wind and solar sources, which represent continuous and realistic disturbances rather than a simple 'rated steady state.' Second, the step disturbance applied at the PCC is a standard 'worst-case' excitation in control theory, covering a wide frequency spectrum (0–30 Hz) to test the controller's recovery capability. Regarding large-signal disturbances such as faults or three-phase unbalance, although they are beyond the current scope of small-signal modeling, the five-degree-of-freedom structure of the FOPID controller provides inherently higher parameter margins than traditional PID, suggesting a strong potential for handling complex grid conditions. Further verification under unbalanced and harmonic scenarios will be the focus of our future work involving hardware-in-the-loop (HIL) testing.

6. Conclusions and Future Outlook

6.1. Conclusions

Aiming at the key technical problems of low-frequency oscillation, insufficient regulation accuracy and multi-objective optimization conflicts at the PCC of hydro–wind–photovoltaic hybrid systems, which are caused by the randomness of wind and photovoltaic output, water-hammer effects of hydro-turbine units and multi-source power coupling, this paper presents a series of studies including system modeling, controller design, optimization algorithm improvement and simulation verification. The core conclusions are as follows:

A complete small-signal transfer function model covering photovoltaic inverters, DFIG, hydro-turbine units and VSC-HVDC converter stations is established, which accurately depicts the impacts of water-hammer effect, multi-source power coupling and low inertia characteristics of power electronic devices on PCC dynamic performance, providing a reliable theoretical modeling basis for oscillation instability prevention and controller design. Among them, the rigid water-hammer model of hydro-turbine units and the integrated transfer function of "control link–electrical main circuit" for VSC-HVDC converter stations effectively improve the accuracy of system dynamic characteristic description.

Caputo-type FOPI and FOPID controllers are designed, breaking through the parameter freedom limitation of traditional integer-order controllers. The FOPI controller adapts to the system nonlinear characteristics through a three-parameter system of "proportional coefficient–integral coefficient–fractional integral order", while the FOPID controller adds differential coefficient and fractional differential order to form a five-parameter regulation framework, which significantly enhances the suppression capability for transient disturbances and low-frequency oscillations. Both controllers achieve high-precision discretization via the Tustin + continued fraction expansion method, meeting the requirements of engineering applications. Specifically, a 5th-order approximation is employed within the frequency range of $[10^{-3}, 10^{3}]$ rad/s. The sampling time T_s is set to 0.01 s to balance calculation accuracy and computational efficiency, ensuring that the approximation error is maintained below 10^{-4}.

A dual-objective optimization framework with ITAE (voltage-tracking accuracy) and ODRI (oscillation instability risk) as objectives is established. The ODRI realizes quantitative evaluation of oscillation instability risk, making up for the deficiency of qualitative analysis in traditional studies. The CMOPSO algorithm is adopted to solve the Pareto-optimal solution set: its multi-population cooperative evolution and elite solution archive mechanism ensure the convergence and diversity of the solution set, effectively resolving the multi-objective conflict between dynamic response and oscillation risk.

Simulation results verify the superiority of the proposed FOPID-CMOPSO joint regulation strategy: compared with traditional PI controllers and other optimization algorithms (MPSOD, SIBEA, and MOEAPC), this strategy can effectively suppress 0.5~2 Hz low-frequency oscillations, with PCC voltage overshoot reduced by more than 40%, oscillation attenuation time shortened by 33%, and ITAE and ODRI indices decreased by 12.58% and 2.47% respectively. Meanwhile, the overshoot and fluctuation amplitude of DC bus voltage are significantly reduced, and the steady-state accuracy is greatly improved, exhibiting superior robustness and comprehensive regulation performance. In terms of engineering application, the proposed FOPID-CMOPSO strategy provides a standardized solution for stability control in high-penetration renewable energy grids: specifically, the ODRI index serves as a practical diagnostic tool for quantifiable oscillation risk assessment in grid operation; meanwhile, the high-performance parameter sets optimized by CMOPSO offer highly reliable initial references for industrial controller tuning under complex coupling

conditions, significantly enhancing the field commissioning efficiency and operational safety of multi-energy complementary systems.

6.2. Future Outlook

Future research can be further advanced from two aspects: theoretical and algorithmic optimization, and engineering scenario expansion. On the one hand, enrich the complexity of system modeling by incorporating multi-source disturbances such as extreme fluctuations in wind and photovoltaic output and equipment aging, and introduce uncertainty-modeling methods. Meanwhile, optimize the online parameter-tuning mechanism of fractional-order controllers by combining deep learning, and improve the convergence speed and global search capability of the CMOPSO algorithm. On the other hand, conduct hardware-in-the-loop experiments and engineering pilot tests, build FPGA/DSP-based digital control platforms to verify the feasibility of the proposed strategy, and extend the developed control and optimization methods to multi-source complementary grid-connected systems integrated with energy storage devices and microgrids, so as to provide technical support for the stability control of more extensive new energy power systems.

Author Contributions: B.T.: Conceptualization, data curation, methodology. W.Y.: methodology, investigation, software, writing—original draft. T.Y.: methodology, investigation, writing—review and editing. R.L.: writing—review and editing. Z.W.: software, visualization. C.L.: visualization, writing—review and editing. All authors have read and agreed to the published version of the manuscript.

Funding: This project is funded by the China Yangtze Power Co., Ltd., No: ZSF2402004.

Data Availability Statement: The data presented in this study are available on request from the corresponding author.

Conflicts of Interest: Authors Bojin Tang and Weiwei Yao are employed by the company Institute of Science and Technology, China Three Gorges Corporation. Authors Teng Yi and Rui Lv are employed by the company China Yangtze Power Co., Ltd. The remaining authors declare that the research was conducted in the absence of any commercial or financial relationships that could be construed as a potential conflict of interest. The authors declare that this study receives funding from China Yangtze Power Co., Ltd. (No: ZSF2402004). The funder is not involved in the study design, collection, analysis, interpretation of data, the writing of this article or the decision to submit it for publication.

References

1. Li, Y.; Hua, X.; Wang, L.; Lv, R.; Ouyang, C.; Zhang, F.; Yuan, F. Optimal Scheduling of Hydro-Thermal-Wind-Solar-Pumped Storage Multi-Energy Complementary Systems Under Carbon-Emission Constraints: A Coordinated Model and SVBABC Algorithm. *Electronics* **2025**, *14*, 4896. [CrossRef]
2. Ye, X.; Chen, Z.; Zhu, T.; Wei, W.; Peng, H. Fast Coordinated Predictive Control for Renewable Energy Integrated Cascade Hydropower System Based on Quantum Neural Network. *Electronics* **2024**, *13*, 732. [CrossRef]
3. Azeem, M.; Malik, T.N.; Muqeet, H.A.; Hussain, M.M.; Ali, A.; Khan, B.; Rehman, A.U. Combined Economic Emission Dispatch in Presence of Renewable Energy Resources Using CISSA in a Smart Grid Environment. *Electronics* **2023**, *12*, 715. [CrossRef]
4. Wang, G.; Zhang, Z.; Lin, J. Multi-energy complementary power systems based on solar energy: A review. *Renew. Sustain. Energy Rev.* **2024**, *235*, 114464. [CrossRef]
5. Jiang, H.; Liu, X.; Zhou, H.; Zhao, Y.; Yao, Z. Multi-time-scale optimal scheduling strategy of electricity-heat-cold-gas integrated energy system considering ladder carbon trading. *Energy Rep.* **2025**, *13*, 4000–4014. [CrossRef]
6. Jia, T.; Shuai, Y.; Wang, F.; Zhang, H.; Yang, D.; Geng, B.; Li, Q.; Wu, Q.; Xu, Y. Empowering modern power systems with thermal energy storage in China: A comprehensive review. *Renew. Sustain. Energy Rev.* **2026**, *235*, 116937. [CrossRef]
7. Song, J.; Wang, Y. Data-driven surrogate modeling and automatic PID tuning of hydropower governors for low-inertia power systems. *Energy Rep.* **2026**, *15*, 109235. [CrossRef]
8. Lalparmawii, R.; Majumder, S.; De, K. Fractional-order control and energy storage strategy for frequency stability in renewable power systems. *J. Energy Storage* **2026**, *153*, 120908. [CrossRef]

9. Rudnik, V.E.; Ufa, R.A.; Malkova, Y.Y. Analysis of low-frequency oscillation in power system with renewable energy sources. *Energy Rep.* **2022**, *8*, 394–405. [CrossRef]
10. Li, C.; Zhang, J.; Zhao, K. Research on Suppression of low-frequency oscillations in power systems based on improved P-LADRC with RBF neural network. *Electr. Power Syst. Res.* **2026**, *253*, 112536. [CrossRef]
11. Han, Y.; Yan, X.; Meng, L.; Sun, Y.; Wu, J. An enhanced solar–coal hybrid power generation system by integrating photovoltaic-powered coal pre-drying. *Energy* **2026**, *349*, 140617. [CrossRef]
12. Gümüş, T.E.; Emiroglu, S.; Yalcin, M.A. Optimal DG allocation and sizing in distribution systems with Thevenin based impedance stability index. *Int. J. Electr. Power Energy Syst.* **2023**, *144*, 108555. [CrossRef]
13. Geng, H.; Yuan, X.; Wan, X.; Ling, X.; Wang, Y. Multi-objective coordination operation of hydro-wind-PV system coupled hybrid pumped storage units. *Electr. Power Syst. Res.* **2026**, *254*, 112635. [CrossRef]
14. Maurya, R.K.; Prasad, D.; Singh, R.P. Cost-effective solution for energy demand supply with grid integrated renewable power systems. *e-Prime—Nexus Electr. Electron. Intell. Eng.* **2026**, *17*, 201170. [CrossRef]
15. Yang, J.; Wu, Q.; Luo, W. Optimized dispatch of integrated energy system based on renewable energy-carbon full-cycle interaction mechanism with dynamic step-wise carbon trading. *Electr. Power Syst. Res.* **2026**, *256*, 112914. [CrossRef]
16. He, K.; Chen, J.; Pan, F.; Wang, B.; Ji, C. Adaptive negative-pressure control system for electric-driven seeding blowers based on a DILPSO-fuzzy PID controller. *Comput. Electron. Agric.* **2025**, *239*, 110833. [CrossRef]
17. Cokmez, E.; Kaya, I. Optimal fractional order PI controller design for time-delayed processes. *Results Control Optim.* **2026**, *22*, 100651. [CrossRef]
18. Ramesh, U.K.; Brahmbhatt, P.R.; Avraamidou, S.; Ganesh, H.S. Neural network and integer programming-based Model Predictive Control for a wastewater treatment process. *J. Process Control* **2026**, *162*, 103717. [CrossRef]
19. Adhikary, B.; Swarnakar, J. A novel approach towards discrete-time realization of fractional-order proportional integral controller. *Commun. Nonlinear Sci. Numer. Simul.* **2026**, *152*, 109322. [CrossRef]
20. Abdolahi, A.; Salehi, J.; Gazijahani, F.S.; Safari, A. Probabilistic multi-objective arbitrage of dispersed energy storage systems for optimal congestion management of active distribution networks including solar/wind/CHP hybrid energy system. *J. Renew. Sustain. Energy* **2018**, *10*, 045502. [CrossRef]
21. Amiryousefi, M.; Dehkordi, A.L.; Elhami, B. Optimizing environmental performance of rice production in semi-arid Iran: An Life Cycle Assessment (LCA)-Multi-Objective Particle Swarm Optimization (MOPSO) approach. *Sustain. Futures* **2026**, *11*, 101645. [CrossRef]
22. Duong, T.L.; Do, T.K. Optimal parameters of the cascade controller PI-PI-FOPID for enhancing load frequency control in interconnected power systems using a modified secretary bird optimization algorithm. *Alex. Eng. J.* **2025**, *132*, 352–368. [CrossRef]
23. Mo, J.; Peng, X.; Ma, X.; Geng, S.; Wen, J. Research on hierarchical coordinated variable-gain frequency regulation strategy for wind farm MMC-LCC grid-connected system. *Int. J. Electr. Power Energy Syst.* **2026**, *177*, 111803. [CrossRef]
24. Ma, T.; Zhang, X.; Xiao, J.; Wang, R.; Ruan, C.; Wang, H. Systematic analysis of a fully renewable tri-generation system based on solar-biomass gasification and chemical looping processes. *Energy* **2026**, *344*, 139999. [CrossRef]
25. Irshad, A.S.; Amin, A.S.; Ilham, A.M.; Elkholy, M.H.; Elias, S.; Senjyu, T. Power capacity enhancement of hydropower plant through the penetration of solar and wind energy. *Int. J. Electr. Power Energy Syst.* **2025**, *169*, 110787. [CrossRef]
26. Ranjbar, S. CART-based wide-area damping controller for inter-area oscillations in bulk power system consisting of WAMS data. *ISA Trans.* **2024**, *153*, 350–363. [CrossRef]
27. Tian, S.; Liu, X. Incorporating advanced machine learning algorithms into solar power forecasting in off-grid hybrid renewable systems. *Electr. Power Syst. Res.* **2025**, *248*, 111979. [CrossRef]
28. Li, J.; Yuan, J.; Yue, X. Optimizing multi-objective hybrid energy systems with pumped hydro storage for enhanced stability and efficiency in renewable energy integration. *Eng. Sci. Technol. Int. J.* **2025**, *69*, 102142. [CrossRef]
29. Mohammadi, Y.; Leborgne, R.C. Improved DR and CBM methods for finding relative location of voltage sag source at the PCC of distributed energy resources. *Int. J. Electr. Power Energy Syst.* **2020**, *117*, 105664. [CrossRef]
30. Nicolini, A.M.; Silveira, P.; Cardinal, R. A data-driven approach for evaluating wind turbine degradation. *Sustain. Energy Technol. Assess.* **2025**, *84*, 104755. [CrossRef]

Disclaimer/Publisher's Note: The statements, opinions and data contained in all publications are solely those of the individual author(s) and contributor(s) and not of MDPI and/or the editor(s). MDPI and/or the editor(s) disclaim responsibility for any injury to people or property resulting from any ideas, methods, instructions or products referred to in the content.